CRYSTAL GROWTH & DESIGN

pubs.acs.org/crystal

Article

A Novel Solid Form of Erlotinib: Synthesis by Heterogeneous Complexation and Characterization by NMR Crystallography

Sean T. Holmes, Ren A. Wiscons, Kerrigan Parks, Sarah Nickel, Halie S. Ankeny, Aaron M. Viggiano, Derek Bedillion, Deben Shoup, Robbie J. Iuliucci, Qiang Wang, Robert W. Schurko,* and Rosalynn Quiñones*

Cite This: *Cryst. Growth Des.* 2025, 25, 3219–3228

Read Online

ACCESS | Metrics & More | Article Recommendations | Supporting Information

ABSTRACT: We describe the synthesis of a novel complex of the anticancer "active pharmaceutical ingredient erlotinib (**ERL**) via heterogeneous nucleation on polished zinc tiles. The resulting product, **ERL$_2$·ZnCl$_2$**, is characterized by single-crystal X-ray diffraction, multinuclear solid-state NMR (ssNMR) spectroscopy, and density functional theory (DFT) calculations. Also characterized are the hydrochloride salt (**ERL·HCl**) and monohydrate free base (**ERL·H$_2$O**) forms of erlotinib. ^{13}C ssNMR spectroscopy is useful for site-by-site assignment and rapid fingerprinting, while also providing preliminary structural interpretations, such as the number of molecules in the asymmetric unit. ^{35}Cl ssNMR can readily differentiate between the chloride ions in **ERL·HCl** and the covalently bonded chlorine in **ERL$_2$·ZnCl$_2$**. ^{15}N ssNMR proves to be critical here because of the large isotropic chemical shift differences between **ERL·H$_2$O**, **ERL·HCl**, and **ERL$_2$·ZnCl$_2$**. The ^{15}N chemical shift tensors are linked directly to differences in structure and bonding with the aid of DFT calculations. Together, these results demonstrate the utility of multinuclear NMR crystallography for the characterization of solid forms of APIs, especially when other analytical techniques face significant challenges.

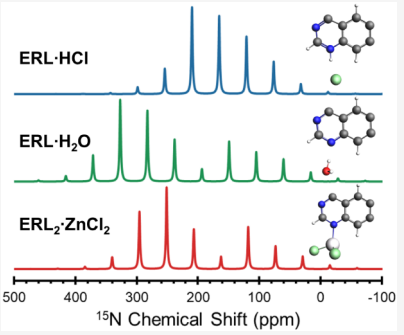

INTRODUCTION

To optimize the physicochemical properties of active pharmaceutical ingredients (APIs), it is essential to explore a diverse array of solid forms, including polymorphs, salts, hydrates, solvates, cocrystals, solid solutions, and amorphous phases.[1−5] Intermolecular interactions (e.g., hydrogen bonding) within a specific solid form significantly influence its properties, including stability, solubility, dissolution rate, and bioavailability. Therefore, understanding the interplay between structure, properties, and pharmacological function is crucial for the rational design of improved drugs.[6−10] However, no universally reliable method exists to generate all of the potential solid forms of an API, making the process inherently *ad hoc* and time-intensive. This challenge is further compounded when analytical and/or spectroscopic techniques fail to reliably distinguish between existing solid forms or confirm the discovery of a novel form.

Due to its promise in treating advanced nonsmall cell lung cancer, erlotinib[11] (*N*-(3-ethynylphenyl)-6,7-bis(2-methoxyethoxy)-4-quinazolinamine (**ERL**, Scheme 1)) is included in the list of essential medicines by the World Health Organization.[12] Erlotinib has garnered significant attention for its medicinal importance, the complexity of synthesizing and characterizing its multiple solid forms, and the associated challenges related to safety and intellectual property. Both free-base[13] and hydrochloride (HCl) salts[14] of erlotinib, as well as their respective hydrates,[15] exhibit polymorphism.[16−22] Additionally,

Scheme 1. Skeletal Representation of Neutral Erlotinib, with the Numbered Nitrogen Atoms Depicted in Various Shades of Blue to Indicate Qualitative Relative Lewis Basicity; N^1 is the most Basic and N^3 is the Least Basic

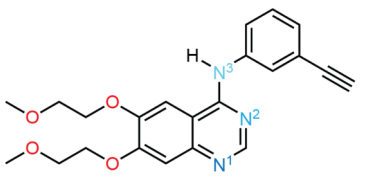

salts (including their polymorphs),[23−26] cocrystals,[15,26] amorphous forms,[27] micro- and nanoparticles,[28,29] and solid dispersions,[27,29−31] have been reported, leading to a complicated landscape of solid forms, most of which have not been structurally characterized. There are also questions regarding optimal synthetic protocols for producing these solid forms, including their reproducibility and the purities of the resulting products. All known forms of erlotinib have very low

Received: February 28, 2025
Revised: April 13, 2025
Accepted: April 16, 2025
Published: April 29, 2025

https://doi.org/10.1021/acs.cgd.5c00268
Cryst. Growth Des. 2025, 25, 3219−3228

aqueous solubilities (i.e., erlotinib is listed as a BCS Class 2 drug),[32−34] which decrease their bioavailability and limit their efficacy in clinical applications. Significant effort has been expended preparing formulations with improved solubility and bioavailability, sometimes involving chemical modification of the erlotinib molecule (e.g., through complexation with phospholipids).[29−31,35−40] Thus, the discovery of novel solid forms of erlotinib, as well as their characterization, could prove fruitful for producing drug formulations with enhanced physicochemical properties.

The variety of erlotinib solid forms is thought to arise, in part, because the N^1 nitrogen atom (Scheme 1) acts as a strong Lewis base: this explains the protonation at N^1 for HCl and oxalate salts,[23,26] as well as why this site serves as a hydrogen-bond acceptor in neutral cocrystals[15,26] and hydrates.[26] In nonprotonated forms, the lone pair on N^1 may also facilitate coordination with metals, as has been observed for metal complexes containing quinazoline or quinoline moieties, which have found applications in medicine, catalysis, optical devices, and other areas.[41−44] To our knowledge, no metal, transition metal, or post-transition metal complexes of erlotinib have been reported—this is surprising, since such complexes may offer advantageous physicochemical properties in comparison to other solid forms, due to their unique electronic and stereochemical properties.

Solid-state NMR (ssNMR) spectroscopy is a powerful tool for characterizing solid forms of APIs since it provides site-specific information on molecular-level structure and bonding;[45−50] as such, it can greatly augment structural determination, providing unique insights into hydrogen atom positions and hydrogen bonding that may not be available from single-crystal X-ray diffraction experiments.[51,52] NMR crystallography (NMRX) techniques, which feature the pairing of ssNMR with quantum chemical calculations using density functional theory (DFT), provide chemical information that is invaluable for the characterization of API solid forms.[53−60] Furthermore, there are cases in which ssNMR can play a key role in the spectral fingerprinting of different solid forms of APIs, optimization of synthetic protocols, identification of products and unreacted educts, and interpretation of structural features in the absence of diffraction data.[46,48] In this respect, 1D and/or 2D ssNMR experiments involving ^{1}H, ^{13}C, and ^{15}N are the most common for characterizing APIs. However, quadrupolar nuclides (nuclear spin, $I > 1/2$) such as ^{35}Cl also have great potential application here, since their ssNMR spectra are extremely sensitive to long-range hydrogen bonding interactions that are often not revealed from chemical shift measurements.[53,61−64] To date, NMRX studies have not been carried out on any solid form of erlotinib; however, for the reasons mentioned above, ssNMR methods are expected to be of great utility for these systems.

In light of this, herein we describe the preparation of a new zinc complex of erlotinib, **ERL$_2$·ZnCl$_2$**, using heterogeneous nucleation on zinc tiles, as well as its structural characterization using single-crystal X-ray diffraction (SCXRD), X-ray photoelectron spectroscopy (XPS), powder X-ray diffraction (PXRD), differential scanning calorimetry (DSC), infrared spectroscopy, ssNMR spectroscopy, and DFT calculations. Two other solid forms of erlotinib, including its monohydrate free base (**ERL·H$_2$O**) and hydrochloride salt (**ERL·HCl**), were also produced and characterized by these methods. Only **ERL·H$_2$O** has a known crystal structure,[26] whereas **ERL·HCl** is referred to as "Form B" in the patent literature.[25] Additionally, attempts were made to isolate and characterize an anhydrous free-base form of erlotinib, **ERL·FB**. We highlight the use of multinuclear ssNMR for the characterization of these solid forms, since it provides insights into structure and bonding that is not available from other techniques.

EXPERIMENTAL AND COMPUTATIONAL DETAILS

Materials. **ERL·HCl** was purchased from ApexBio Tech (>99%), whereas **ERL·FB** was purchased from LC Laboratories (>99%). **ERL·H$_2$O** was obtained by recrystallizing **ERL·FB** from H_2O.[26] **ERL$_2$·ZnCl$_2$** was prepared by recrystallization on Zn tiles (Goodfellow Cambridge Ltd., 99.95+%) that were sanded, cleaned, and cut into 1 cm^2 squares. A 16 mM **ERL·HCl** solution in methanol was prepared using sonication and heat. The Zn tiles were placed into well plates and 500 μL of the **ERL·HCl** solution was added to each. The solution was left to evaporate slowly at room temperature by covering it with aluminum foil. Following solvent evaporation, the crystals that formed at the top of each tile were carefully removed for further analysis.

Single-Crystal X-Ray Diffraction. SCXRD images were collected using a Rigaku XtaLAB Synergy-i X-ray diffractometer configured in a kappa goniometer geometry. The diffractometer, which is equipped with a low-temperature device and a PhotonJet-S microfocus Cu source (λ = 1.54187 Å), was operated at 50 kV and 1 mA. X-ray intensities were measured at 150 K with the Bantam detector placed 44.00 mm from the sample. The data were processed with CrysAlisPro version 41_64.117a (Rigaku Oxford Diffraction) and corrected for absorption. The structures were determined in OLEX2[65] using SHELXT[66] and refined using SHELXL.[67] All non-hydrogen atoms were refined anisotropically with hydrogen atoms placed at idealized positions except in cases of significant positional disorder. Single crystals were mounted on a 150 μm MiTeGen MicroMount using mineral oil.

Powder X-Ray Diffraction. PXRD patterns were collected using a Rigaku XtaLAB Synergy-i X-ray diffractometer configured in a kappa goniometer geometry. The diffractometer is equipped with a low-temperature device and a PhotonJet-S microfocus Cu source (λ = 1.54187 Å) and operated at 50 kV and 1 mA. X-ray intensities were measured at room temperature with the Bantam detector placed 44.00 mm from the sample. All images were collected with a continuous ϕ-rotation scan with a 200 s exposure time. Due to the instrument configuration, minimal sample sizes were required (sufficient sample to pack into a sphere 150−200 μm in diameter). This data collection strategy also minimizes the effects of preferred orientation. The images were processed into diffraction patterns using CrysAlisPro version 41_64.117a (Rigaku Oxford Diffraction). Samples were mounted on a 150 μm MiTeGen MicroMount using mineral oil. Additional PXRD patterns were obtained using a PANalytical X'Pert Pro MPD powder X-ray diffractometer with Cu $K\alpha$ X-ray source operating at 45 kV and 40 mA power in the Bragg−Brentano geometry. The patterns were collected over a 2θ range of 5° to 80° at a step size of 0.017° with a solid-state X-ray detector.

Solid-State NMR Spectroscopy. ssNMR experiments at B_0 = 9.4 T were conducted using a Varian Inova spectrometer and Oxford magnet, with Larmor frequencies of $\nu_0(^1\text{H})$ = 399.8 MHz, $\nu_0(^{13}\text{C})$ = 100.5 MHz, and $\nu_0(^{15}\text{N})$ = 40.5 MHz. High-field ^{35}Cl ssNMR experiments were conducted at the National High Magnetic Field Laboratory using a Bruker Avance NEO console and a home-built 21.1 T ultrawide bore magnet,[68] with Larmor frequencies of $\nu_0(^1\text{H})$ = 894.52 MHz and $\nu_0(^{35}\text{Cl})$ = 87.64 MHz. Additional experiments were conducted at 18.8 T using a Bruker Avance III spectrometer with Larmor frequencies of $\nu_0(^1\text{H})$ = 800.1 MHz and $\nu_0(^{35}\text{Cl})$ = 78.4 MHz. All ssNMR spectra were processed and analyzed using the ssNake v1.4 software package.[69] Further details of the ssNMR experiments are provided in Supplement S1. All pulse sequences and recommended calibration parameters and standards are available from the authors by request or at https://github.com/rschurko.

Quantum Chemical Calculations. All quantum chemical calculations were performed using DFT methods. Refinements of crystal structures were performed using the CASTEP module within

https://doi.org/10.1021/acs.cgd.5c00268
Cryst. Growth Des. 2025, 25, 3219−3228

Materials Studio 2020.[70] Calculations of NMR interaction tensors were performed using Amsterdam Density Functional 2021.[71] Details of these calculations are provided in Supplement S2.

RESULTS AND DISCUSSION

Synthesis and Characterization of $ERL_2{\cdot}ZnCl_2$. A 16 mM solution of **ERL·HCl** in methanol was placed on polished square zinc tiles with a surface area of 1 cm^2 and allowed to evaporate under ambient conditions. This yielded white crystals on the surface that were carefully removed for further analysis. It was initially assumed that the novel form prepared in this manner was simply another polymorph, hydrate, or salt of erlotinib, adding to the abundance of known solid forms. However, it initially proved difficult to obtain suitable crystals for analysis by SCXRD. Instead, other analytical characterization methods were pursued.

The white crystals were initially characterized by solution NMR, DSC, and XPS. ^{1}H and ^{13}C NMR spectra of the sample dissolved in DMSO-d_6 indicate the presence of the free base, via comparison to analogous spectra of **ERL·H_2O** and **ERL·HCl** (Figure S5a,b). DSC scans revealed thermal behavior more akin to that of **ERL·HCl** than **ERL·H_2O** (Supplement S3). XPS revealed the presence of zinc and chlorine, suggesting the potential formation of a zinc complex (Supplement S4). Infrared spectra were also acquired, which are useful for fingerprinting (Supplement S5). Collectively, these data encouraged further analysis of the sample, as described below.

Single-Crystal X-Ray Diffraction. Selection of the best crystals from the sample led to the determination of the structure of a novel complex, **$ERL_2{\cdot}ZnCl_2$**, using SCXRD at 150 K (Figure 1, Table 1). The crystal structure is available

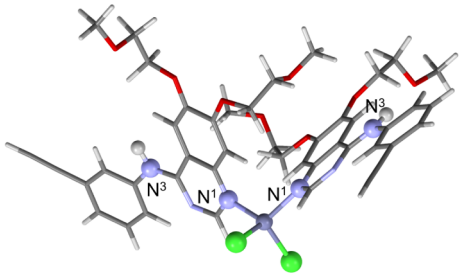

Figure 1. Crystal structure of **$ERL_2{\cdot}ZnCl_2$** viewed along the crystallographic *b*-axis, as determined by single-crystal X-ray diffraction and subsequent plane-wave DFT geometry optimization. The nitrogen atoms N^1 and N^3 are indicated.

from the Cambridge Structural Database under deposition number 2403615. ORTEP images of the crystal structure are provided in Figure S6. **$ERL_2{\cdot}ZnCl_2$** crystallizes in the $P2_1/n$ space group with $Z' = 1$ and $Z = 4$, and features a pseudotetrahedral Zn center bound to two Cl atoms and two molecules of erlotinib through N^1. Zn−Cl bond lengths, r(Zn···Cl), of 2.275 Å and 2.276 Å (DFT geometry optimized), are slightly shorter than those of $ZnCl_2$ (2.304 Å).[72] There are two N^3−H···Cl hydrogen bonds with distances, $r(N^3{-}H{\cdots}Cl)$, of 2.558 and 2.584 Å (geometry optimized structure). Finally, there is some degree of disorder evident in two of the four of the methoxy moieties.

Powder X-Ray Diffraction. PXRD (Figure 2) was used to investigate the purity of the **$ERL_2{\cdot}ZnCl_2$** samples crystallized via the heterogeneous nucleation method. Given the small sample size, PXRD patterns were extracted from continuous φ-rotation diffraction images collected using a SCXRD instrument, revealing that **$ERL_2{\cdot}ZnCl_2$** exists uniformly throughout the bulk microcrystalline sample, as confirmed by comparison to a simulated PXRD pattern based on the new crystal structure. **ERL·H_2O** was demonstrated to be pure by similar means,[23,26] whereas PXRD provides a fingerprint for **ERL·HCl**.

Table 1. Single-Crystal X-Ray Diffraction Data and Refinement Parameters for $ERL_2{\cdot}ZnCl_2$

Crystal Data	
Chemical formula	$C_{44}H_{46}N_6O_8ZnCl_2$
M_r (amu)	923.16
Crystal system, space group	Monoclinic, $P2_1/n$
Temperature (K)	150(1)
a, *b*, *c* (Å)	11.2148 (7), 23.9974 (13), 16.2008 (9)
β (°)	100.221
V (Å^3)	4290.87
Z	4
Radiation type	Cu Kα
Crystal size (mm)	0.028 × 0.054 × 0.115
Data collection	
Diffractometer	XtaLAB Synergy, Single source at home/near, HyPix3000
Absorption correction	Multiscan CrysAlis PRO 1.171.41.117a (Rigaku Oxford Diffraction, 2021) empirical absorption correction using spherical harmonics, implemented in SCALE3 ABSPACK scaling algorithm.
Tmin, Tmax	0.945, 1.000
No. of measured, independent, and observed [$I > 2\sigma(I)$] reflections	22327, 7696, 4859
Rint	0.061
$(\sin\theta/\lambda)_{max}$ (Å^{-1})	0.603
Refinement Information	
$R[F^2 > 2\sigma(F^2)]$, $wR(F^2)$, S	0.0643, 0.1707, 1.037
No. of reflections	7696
No. of parameters	575
H atom treatment	H atoms treated by a mixture of independent and constrained refinement
$\Delta\rho_{max}$, $\Delta\rho_{min}$ (e Å^{-3})	0.54, −0.62

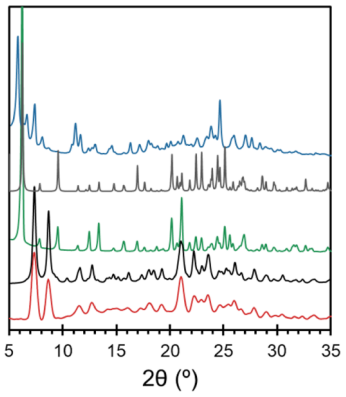

Figure 2. Powder X-ray diffraction patterns for three solid forms of erlotinib, including **ERL·HCl** (blue), **ERL·H_2O** (green), and **$ERL_2{\cdot}ZnCl_2$** (red). Simulated patterns based on the known crystal structures of **ERL·H_2O** and **$ERL_2{\cdot}ZnCl_2$** are shown in gray and black, respectively.

Solid State NMR Spectroscopy. In this section, we discuss the application of ^{13}C, ^{15}N, and ^{35}Cl ssNMR for the

https://doi.org/10.1021/acs.cgd.5c00268
Cryst. Growth Des. 2025, 25, 3219−3228

structural characterization and spectral fingerprinting of **ERL$_2$·ZnCl$_2$**, **ERL·H$_2$O**, and **ERL·HCl**. Quantum chemical calculations are used to provide site assignments and assess the impact of molecular-level structure and bonding on chemical shift and electric field gradient (EFG) tensors.[73]

^{1}H−^{13}C CP/MAS spectra reveal significant differences between each solid form (Figure 3). The number of peaks in

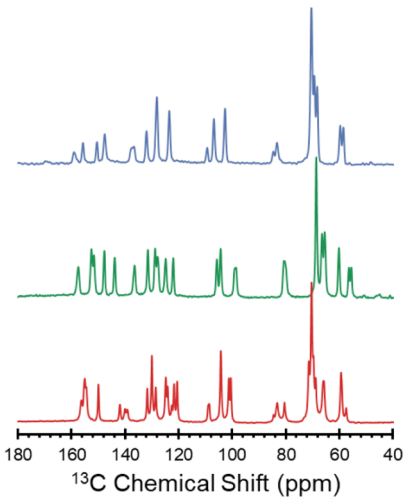

Figure 3. ^{1}H−^{13}C CP/MAS spectra (ν_{rot} = 10−12 kHz) of **ERL·HCl** (blue), **ERL·H$_2$O** (green), and **ERL$_2$·ZnCl$_2$** (red) acquired at 9.4 T.

the spectrum of **ERL$_2$·ZnCl$_2$** is greater than the expected 22 peaks due to the presence of two erlotinib molecules in the asymmetric unit. Differences are evident in the ^{13}C chemical shifts associated with the quinazoline groups due to variations in their structure and bonding at the N^1 sites. The ^{13}C chemical shifts of the ethynylphenyl ring are similarly influenced. Assignments of ^{13}C peaks were assisted by DFT calculations of isotropic chemical shifts; however, these are only approximate, especially when differences between chemical shifts are very small (i.e., less than 2 ppm): a summary of computational results is given in Figure S7. We note that ^{1}H−^{13}C CP/MAS experiments may be a viable pathway for monitoring the interconversion between solid forms *in situ*. For example, our attempts to isolate a pure phase of **ERL·FB** were hindered by its conversion to **ERL·H$_2$O**—this process was monitored *in situ* for a sample of **ERL·FB** packed in a 4.0 mm o.d. rotor over 48 h, demonstrating partial conversion to **ERL·H$_2$O** (Figure S8).

Differences in structure and bonding between the solid forms of erlotinib are prominently reflected in variations of the ^{15}N isotropic chemical shifts measured from the ^{1}H−^{15}N CP/MAS NMR spectra, collected at natural abundance (n.a.(^{15}N) = 0.368%, Figure 4). The spectra for **ERL·H$_2$O** and **ERL·HCl** each feature three peaks, whereas that of **ERL$_2$·ZnCl$_2$** features six peaks due to the presence of two ERL molecules in the complex (*N.B.*: splitting of the N^1 peaks is only *ca.* 20 Hz). **ERL·HCl**, which is protonated at the N^1 site, has δ_{iso}(N^1) = 165.2 ppm, whereas the nonprotonated **ERL·H$_2$O** has δ_{iso}(N^1) = 238.0 ppm. Between these extremes, **ERL$_2$·ZnCl$_2$**, which features N^1 coordination with Zn, has δ_{iso}(N^1) = 206.7 ppm. The variation in the δ_{iso} for the arylamine nitrogen N^3 follows the reverse trend (**ERL·HCl** > **ERL$_2$·ZnCl$_2$** > **ERL·H$_2$O**), although the differences are smaller (*ca.* 16 ppm)—this is unsurprising since N^3 is not within a conjugated heterocycle. In

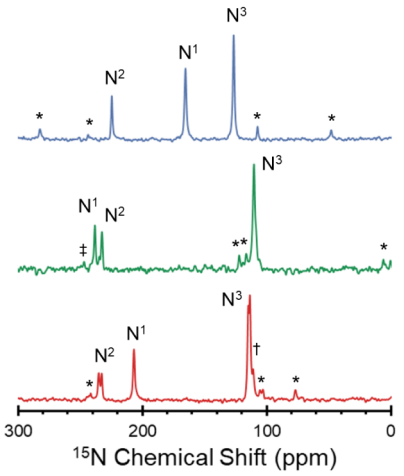

Figure 4. High resolution ^{1}H−^{15}N CP/MAS spectra (ν_{rot} = 4.70 − 5.25 kHz) of **ERL·HCl** (blue), **ERL·H$_2$O** (green), and **ERL$_2$·ZnCl$_2$** (red) acquired at 9.4 T. Spinning sidebands are marked with an asterisks. The spectrum for **ERL$_2$·ZnCl$_2$** shows a doubling of the N^2 and N^3 peaks due to the presence of two molecules in the asymmetric unit. A small amount of an unidentified impurity phase appears in the baseline of the spectrum for **ERL$_2$·ZnCl$_2$** next to the N^3 peak (†). There is also a small impurity in the spectrum of spectrum for **ERL·H$_2$O** (‡) near the N^1 peak, likely corresponding to a polymorph or an anhydrous phase of ERL.

contrast, there is less variability in the values of δ_{iso}(N^2) (a range of *ca.* 10 ppm), in part because this site is not involved in hydrogen bonding or zinc coordination.

The nitrogen chemical shift tensors, obtained from ^{1}H−^{15}N CP/MAS NMR spectra obtained under conditions of slow MAS (Figure 5, Table 2 and Figure S9a−c), reflect the

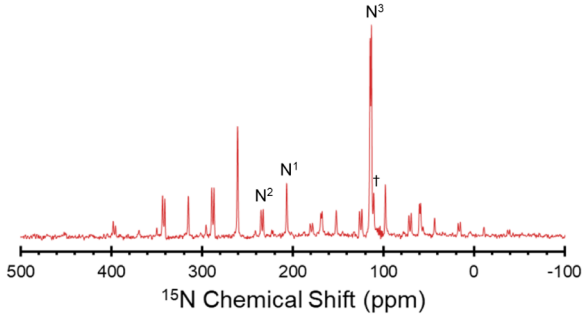

Figure 5. Slow-spinning ^{1}H−^{15}N CP/MAS (ν_{rot} = 2.2 kHz) spectrum of **ERL$_2$·ZnCl$_2$** (red) acquired at 9.4 T. A small amount of an unidentified impurity phase appears in the baseline of the spectrum next to the N^3 peak (†).

electronic structures of the erlotinib molecules in each solid form to a greater degree than the isotropic shifts. The large variations in δ_{iso}(N^1) in the different bonding environments are due to differences in chemical shift anisotropy (CSA) that stem from disparities in all three principal components, with δ_{11} and δ_{22} exhibiting the largest differences; notably, δ_{22} varies by as much as *ca.* 150 ppm between **ERL·H$_2$O** (331 ppm) and **ERL·HCl** (184 ppm), with **ERL$_2$·ZnCl$_2$** falling between these (290 ppm). The ^{15}N chemical shift tensors for the arylamine N^3 sites also reflect changes in electronic structure due to the bonding environment of N^1. In part, this is because the arylamine lone-pair electrons are delocalized in the quinazoline

https://doi.org/10.1021/acs.cgd.5c00268
Cryst. Growth Des. 2025, 25, 3219−3228

Table 2. Experimental ^{15}N Chemical Shift Tensors for Three Solid Forms of ERL[abc]

		δ_{iso} (ppm)	δ_{11} (ppm)	δ_{22} (ppm)	δ_{33} (ppm)	Ω (ppm)	κ
			N1				
ERL·HCl		165.2	276(3)	184(2)	36(2)	240	0.24
ERL·H_2O		238.0	380(8)	331(6)	3(5)	377	0.74
ERL_2·$ZnCl_2$	Avg. M1 and M2[d]	206.7	326(7)	290(5)	5(5)	321	0.78
			N2				
ERL·HCl		224.6	396(5)	299(4)	−21(3)	417	0.54
ERL·H_2O		232.4	405(5)	305(4)	−12(3)	417	0.52
ERL_2·$ZnCl_2$	M1	232.7	416(14)	305(10)	−23(9)	439	0.49
	M2	235.0	421(6)	311(4)	−26(4)	447	0.51
			N3				
ERL·HCl		126.5	201(2)	117(2)	62(2)	139	−0.21
ERL·H_2O		110.1	163(2)	97(2)	70(2)	93	−0.42
ERL_2·$ZnCl_2$	M1	113.3	184(2)	100(2)	56(2)	128	−0.31
	M2	114.8	186(2)	100(2)	59(2)	127	−0.35

[a]Theoretical chemical shift tensors were obtained from calculations on XRD-derived structural models refined using dispersion-corrected plane-wave DFT calculations. The magnetic shielding tensors were calculated at the PBE0 level. [b]The principal components of the chemical shift tensors are defined using the frequency-ordered convention, with $\delta_{11} \geq \delta_{22} \geq \delta_{33}$. The isotropic chemical shift, span, and skew are given by $\delta_{iso} = (\delta_{11} + \delta_{22} + \delta_{33})/3$, $\Omega = \delta_{11} - \delta_{33}$, and $\kappa = 3(\delta_{22} - \delta_{iso})/\Omega$, respectively. [c]The uncertainties in the principal components of the chemical shift tensors (in parentheses) depend on many factors, including signal-to-noise, overlapping peaks, the number of spinning sidebands, and the size of the chemical shift anisotropy. The average uncertainty was estimated to be ca. 4 ppm, with a few extreme values extending over 10 ppm (these large uncertainties correspond to the nitrogen atoms in **ERL_2·$ZnCl_2$** with unresolved peaks in their corresponding spectra). [d]These values represent averages for two nitrogen atoms that could not be differentiated.

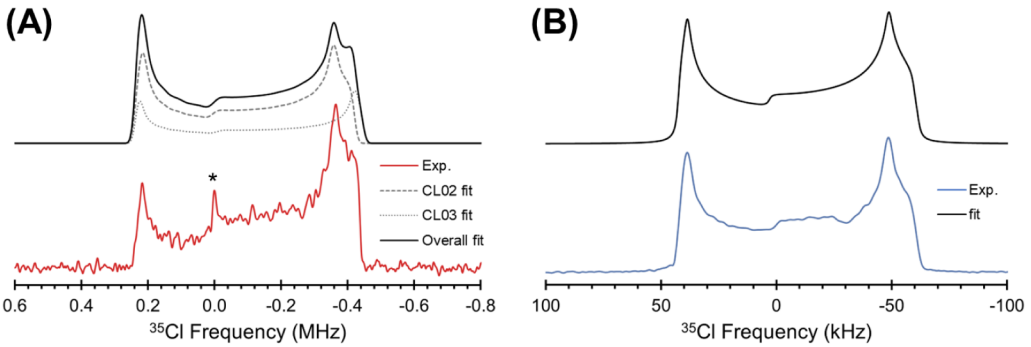

Figure 6. (A) A ^{35}Cl ssNMR spectrum of **ERL_2·$ZnCl_2$** acquired at 21.1 T using the WURST-CPMG pulse sequence (red), along with a simulated pattern (black) and a deconvolution of the pattern into the two underlying components, corresponding to the two types of chlorine atoms (CL02 and CL03). The asterisk indicates an additional signal that may correspond to a small amount of **ERL·HCl**, or a polymorph thereof. (B) A ^{35}Cl ssNMR spectrum of **ERL·HCl** acquired at 18.8 T using the CPMG pulse sequence (blue), along with a simulated pattern (black).

ring, as evidenced by the fact that the arylamine is coplanar with the quinazoline ring. However, because the chemical shift span of the arylamines is smaller than that observed for aromatic nitrogen atoms N^1 and N^2, the variation is less pronounced. The most significant change is again observed for δ_{11}, where the difference between **ERL·HCl** and the **ERL·H_2O** is 38 ppm. As anticipated, the value of δ_{11} for **ERL_2·$ZnCl_2$** falls between these. The variation in the principal values of N^2 between the different forms is comparatively modest.

Nitrogen magnetic shielding tensors can now be calculated with a high degree of accuracy; as such, they are increasingly used for site assignments and interpretation of electronic effects on molecular structure.[58,59,74−77] Experimental and computed ^{15}N chemical shift tensors are summarized in Figure S10. Agreement between calculation and experiment is good, with chemical shift distances (see Supplement S2)[78] ≤10 ppm for each nitrogen site.

One important insight provided by DFT calculations is the orientation of the principal components of the ^{15}N chemical shift tensors with respect to the molecule. This can be demonstrated by considering the orientation of the ^{15}N chemical shift tensor for N^1, since it features the most variability between the three solid forms (Figure S11). In **ERL·H_2O**, δ_{11} and δ_{22} reside in plane of the quinazoline ring with δ_{22} pointing in general direction of the N^1···H hydrogen bonding axis with the water molecule. In **ERL_2·$ZnCl_2$**, δ_{11} and δ_{22} are also in the plane of ring, but with δ_{11} pointing in the general direction of the N^1−Zn coordinating bonding axis. In both cases, δ_{33} is oriented perpendicular to the ring, which reflects why there is less variability in this principal component. Furthermore, calculations on systems with known structures lend insight into systems with unknown structures, such as **ERL·HCl**. In the protonated species **ERL·HCl**, δ_{11} is likely aligned along (or near) the N^1−H···Cl^- hydrogen bonding axis. From this observation, it is clear that the principal component of the ^{15}N chemical shift tensor that is oriented perpendicular to the relevant bonding axis follows the trend **ERL·H_2O** (δ_{11} = 380 ppm) > **ERL_2·$ZnCl_2$** (δ_{22} = 290 ppm) > **ERL·HCl** (δ_{22} = 184 ppm). Analysis of the ^{15}N magnetic shielding tensors of the arylamine N^3 sites provide complementary structural information (Figure S12). For each solid form, δ_{33} is similarly oriented along or near the N−H

https://doi.org/10.1021/acs.cgd.5c00268
Cryst. Growth Des. 2025, 25, 3219−3228

bonding axis, with δ_{22} approximately within the plane of the molecule, and δ_{11} perpendicular to it. Here, it is again clear that the principal components of the ^{15}N chemical shift tensor that are most reflective of differences in bonding are those perpendicular to the bonding axis. For **ERL·HCl**, this further indicates that N^3 must participate in N^3–H···Cl^- hydrogen bonding.

An ultrawideline ^{35}Cl spectrum of **ERL$_2$·ZnCl$_2$**, acquired at B_0 = 21.1 T (Figure 6A), features a single central-transition (CT, +1/2 ↔ −1/2) powder pattern with a breadth of *ca.* 725 kHz. The spectrum was acquired using the WURST-CPMG pulse sequence,[79,80] which affords broadband excitation and refocusing of spin polarization, as well as T_2-based signal enhancement, both of which are essential for acquiring spectra with ultrawideline powder patterns, which can range in breadth from 250 kHz to upward of 10 MHz.[81] Unfortunately, **ERL$_2$·ZnCl$_2$** has a small $T_2^{eff}(^{35}Cl)$ constant, resulting in a short CPMG echo train and correspondingly low signal-to-noise ratio (Figure S13); however, there is enough detail in the spectrum to warrant simulation and analysis.

The ^{35}Cl ssNMR spectrum of **ERL$_2$·ZnCl$_2$** indicates the presence of two overlapping patterns, corresponding to the two crystallographically and magnetically distinct chlorine atoms (see Figure S14 for additional evidence of this, based on a spectrum with much higher resolution but lower signal-to-noise). The powder patterns are dominated by the second-order quadrupolar interaction, with no clear indication of chemical shift anisotropy. Numerical fits yield the δ_{iso} values, quadrupolar coupling constants (C_Q), and asymmetry parameters (η_Q), which are summarized in Table 3 along with values derived from DFT calculations. The low values of η_Q indicate axially symmetric EFG tensors, which are consistent with chlorine atoms participating in terminal zinc-chlorine bonding. The values of C_Q are similar to those in previous reports for Cl atoms in transition metal and post-transition metal compounds, which typically fall within the range of *ca.* 10–30 MHz, with the large range of values reflecting the diverse natures of metal–ligand bonds.[82−88] DFT calculations show that the sign of C_Q is negative for both chlorine atoms, with the EFG tensor oriented such that its largest principal component, V_{33}, is approximately along the Zn–Cl bonding axis; therefore, the EFG diminishes along this axis away from the nucleus. From these calculations, we assign the ^{35}Cl ssNMR narrower powder pattern (C_Q = 20.4 MHz) to the crystallographic site CL02, and the broader pattern (C_Q = 21.2 MHz) to CL03. The differences in the EFG tensors do not appear to be related to the Zn–Cl bond lengths (because these are nearly identical), and likely result from subtle variations in hydrogen bonding with N^3. The values of C_Q are slightly smaller than that of the chlorine atom in $ZnCl_2$ (C_Q = 22.10 MHz, Figure S15), possibly indicating that complexation with erlotinib decreases the covalency of the Zn–Cl bonds;[89] however, the chlorine atoms in $ZnCl_2$ reside in a bridging environment (i.e., each is bound to two zinc atoms), resulting in a nonaxial ^{35}Cl EFG tensor. (*N.B.*: the analysis of the ^{35}Cl EFG tensor of $ZnCl_2$ will be the subject of an upcoming study from one of our laboratories.) There is also an additional narrow feature in the pattern (marked by an asterisk) that may be indicative of a small quantity of a chloride salt in the sample.

In contrast, the ^{35}Cl spectrum of **ERL·HCl** (Figure 6B), obtained at 18.8 T using a CPMG pulse sequence,[90] reveals a comparatively narrow pattern (*ca.* 105 kHz at 18.8 T), which is consistent with a chloride ion participating only in intermolecular hydrogen bonding, rather than covalent bonding.[61,63,64,91] The values of C_Q and η_Q for **ERL·HCl** are summarized in Table 3, with a more complete analysis summarized in Table S2. Although the crystal structure of this polymorph is unknown, the high value of C_Q (7.48 MHz) and low value of η_Q (0.13) are consistent with a chloride ion featuring either a single short hydrogen bond (i.e., less than 2.2 Å), or two short contacts separated by *ca.* 180°—the latter configuration of hydrogen bonds is observed in the other known polymorph (as depicted in Figure S16).[23] Furthermore, the analysis of the ^{15}N magnetic shielding tensors of N^1 and N^3 in **ERL·HCl** (*vide supra*) suggest that both of these sites participate in N–H···Cl^- hydrogen bonding. These insights into the hydrogen bonding network of **ERL·HCl** may prove critical in future crystallographic investigations, possibly involving NMR-guided crystal structure prediction[53,56] and/or NMR-guided Rietveld refinement methods.[92]

Table 3. Experimental and Calculated ^{35}Cl Chemical Shifts and EFG Tensors for the Two Chlorine Atoms in ERL$_2$·ZnCl$_2$ and the Single Chlorine Atom in ERL·HCl[a,b,c,d]

Chlorine Site		δ_{iso} (ppm)	C_Q (MHz)	η_Q
ERL$_2$·ZnCl$_2$ (CL02)	Exp.	50(100)	20.4(3)	0.06(2)
	Calc.	−21	−22.38	0.08
ERL$_2$·ZnCl$_2$ (CL03)	Exp.	−100(100)	21.2(3)	0.03(2)
	Calc.	−38	−22.84	0.06
ERL·HCl	Exp.	74(5)	7.48(6)	0.13(3)
	Calc.	n/a[e]	n/a[e]	n/a[e]

[a]Theoretical chemical shifts and EFG tensors were obtained from calculations on XRD-derived structural models refined using dispersion-corrected plane-wave DFT calculations. [b]Chemical shifts are reported relative to 0.1 M NaCl. Calculated values are converted to the chemical shift scale by setting the computed shielding for L-histidine HCl·H_2O to 34.5 ppm. [c]The experimental uncertainties in the last digit for each value are indicated in parentheses. [d]The principal components of the EFG tensors are defined such that $|V_{33}| \geq |V_{22}| \geq |V_{11}|$. The quadrupolar coupling constant and asymmetry parameter are given by $C_Q = eQV_{33}/h$, and $\eta_Q = (V_{11} - V_{22})/V_{33}$, respectively. The sign of C_Q cannot be determined from the experimental ^{35}Cl spectra. [e]Since there is not a known crystal structure for **ERL·HCl**, no calculated NMR interaction tensors are reported.

CONCLUSIONS

A novel solid form of the anticancer drug erlotinib was synthesized through complexation on polished zinc tiles. Analysis by single-crystal XRD revealed the formation of a metal-API complex for the form **ERL$_2$·ZnCl$_2$**. This novel API solid form, along with **ERL·H_2O** and **ERL·HCl**, were characterized using a multinuclear NMR crystallography approach. This approach features experimentation on the NMR-active nuclides ^{13}C, ^{15}N, and ^{35}Cl, and proves to be exceptionally useful for the structural characterization of API solid forms that are difficult to analyze through other methods. In addition to providing spectral fingerprints that serve as to unambiguously identify the solid form, these NMR spectra also provide a wealth of chemical information that is linked to crystal structure, hydrogen bonding, and API-metal complexation. In particular, we find that ^{15}N chemical shift tensors are exquisitely sensitive to electronic structure resulting from differences in protonation state, intermolecular noncovalent interactions such as hydrogen bonding, and the bonding

https://doi.org/10.1021/acs.cgd.5c00268
Cryst. Growth Des. 2025, 25, 3219−3228

between nitrogen and zinc atoms. The variation in ^{15}N chemical shift tensors was reproduced using state-of-the-art DFT calculations, which provide their key relationships with molecular-level structure and bonding, and even offer significant insight in cases where crystal structures are unknown. Together, these techniques lend insight into the crystal structures and chemical bonding within the solid forms of erlotinib, provide an avenue for the discovery of additional solid forms of erlotinib, suggest future applications to the characterization of a diverse array of solid forms of APIs using multinuclear NMR crystallography, and could aid in improving crystal structure prediction routines for multicomponent API solid forms.

■ ASSOCIATED CONTENT

Supporting Information

The Supporting Information is available free of charge at https://pubs.acs.org/doi/10.1021/acs.cgd.5c00268.

Additional experimental and computational details; DSC analysis; XPS analysis; IR analysis; solution-state ^{1}H and ^{13}C NMR analysis; additional details of the crystal structure; additional multinuclear ssNMR analysis (PDF)

Accession Codes

Deposition Number 2403615 contains the supplementary crystallographic data for this paper. These data can be obtained free of charge via the joint Cambridge Crystallographic Data Centre (CCDC) and Fachinformationszentrum Karlsruhe Access Structures service.

■ AUTHOR INFORMATION

Corresponding Authors

Robert W. Schurko − *Department of Chemistry & Biochemistry, Florida State University, Tallahassee, Florida 32306, United States; National High Magnetic Field Laboratory, Tallahassee, Florida 32310, United States;* orcid.org/0000-0002-5093-400X; Email: rschurko@fsu.edu

Rosalynn Quiñones − *Department of Chemistry, Marshall University, Huntington, West Virginia 25755, United States;* orcid.org/0000-0001-8455-4358; Email: quinonesr@marshall.edu

Authors

Sean T. Holmes − *Department of Chemistry & Biochemistry, Florida State University, Tallahassee, Florida 32306, United States; National High Magnetic Field Laboratory, Tallahassee, Florida 32310, United States;* orcid.org/0000-0002-5821-9641

Ren A. Wiscons − *Department of Chemistry, Amherst College, Amherst, Massachusetts 01002, United States;* orcid.org/0000-0002-8281-0343

Kerrigan Parks − *Department of Chemistry, Marshall University, Huntington, West Virginia 25755, United States*

Sarah Nickel − *Department of Chemistry, Marshall University, Huntington, West Virginia 25755, United States*

Halie S. Ankeny − *Department of Chemistry, Washington & Jefferson College, Washington, Pennsylvania 15301, United States*

Aaron M. Viggiano − *Department of Chemistry, Washington & Jefferson College, Washington, Pennsylvania 15301, United States*

Derek Bedillion − *Department of Chemistry, Washington & Jefferson College, Washington, Pennsylvania 15301, United States*

Deben Shoup − *Department of Chemistry, Marshall University, Huntington, West Virginia 25755, United States*

Robbie J. Iuliucci − *Department of Chemistry, Washington & Jefferson College, Washington, Pennsylvania 15301, United States;* orcid.org/0000-0001-6714-1842

Qiang Wang − *Shared Research Facilities, West Virginia University, Morgantown, West Virginia 25606, United States*

Complete contact information is available at: https://pubs.acs.org/10.1021/acs.cgd.5c00268

Author Contributions

The manuscript was written through contributions from all authors. All authors have given approval to the final version of the manuscript.

Notes

The authors declare no competing financial interest.

■ ACKNOWLEDGMENTS

This work was funded by the NASA West Virginia Space Grant Consortium (Training Grants NNX15AI01H and 80NSSC20M0055), the West Virginia Higher Education Policy Commission (HEPC.dsr.18.7. and dsr.20.16 amend. 1.1), a Research Challenge Grant (RCG23-009), the Marshall University Research Corporation (MURC) for the Undergraduate Creative Discovery Research Scholar and John Marshall University Scholars awards, and the Department of Chemistry at Marshall University. R.W.S. and S.T.H. thank the Department of Energy Basic Energy Sciences (DE-SC0022310), Florida State University, and the National High Magnetic Field Laboratory for funding portions of this research. The National High Magnetic Field Laboratory is supported by the National Science Foundation (NSF) through NSF/DMR-1644779 and NSF/DMR-2128556, and the State of Florida. R.J.I. acknowledges support from the National Science Foundation (NSF MRI CHE-1726824 and NSF REU CHE-2244151). We thank Aakriti Damai and Taylor Maddox for collecting preliminary data for this project. We also thank Dr. Adam Matzger (University of Michigan) for assistance with Raman spectroscopy.

■ REFERENCES

(1) Datta, S.; Grant, D. J. W. Crystal structures of drugs: advances in determination, prediction and engineering. *Nat. Rev. Drug Discovery* **2004**, *3*, 42−57.

(2) Pindelska, E.; Sokal, A.; Kolodziejski, W. Pharmaceutical cocrystals, salts and polymorphs: advanced characterization techniques. *Adv. Drug Delivery Rev.* **2017**, *117*, 111−146.

(3) Karpinski, P. H. Polymorphism of active pharmaceutical ingredients. *Chem. Eng. Technol.* **2006**, *29*, 233−237.

(4) Byrn, S. R.; Zografi, G.; Chen, X. Solvates and hydrates. In *Solid State Properties of Pharmaceutical Materials*; John Wiley & Sons, 2017, pp. 38−47.

(5) Healy, A. M.; Worku, Z. A.; Kumar, D.; Madi, A. M. Pharmaceutical solvates, hydrates and amorphous forms: a special emphasis on cocrystals. *Adv. Drug Delivery Rev.* **2017**, *117*, 25−46.

(6) Jones, W.; Motherwell, W. D. S.; Trask, A. V. Pharmaceutical cocrystals: an emerging approach to physical property enhancement. *MRS Bull.* **2006**, *31*, 875−879.

(7) Babu, N. J.; Nangia, A. Solubility advantage of amorphous drugs and pharmaceutical cocrystals. *Cryst. Growth Des.* **2011**, *11*, 2662−2679.

(8) Kuminek, G.; Cao, F.; Bahia de Oliveira da Rocha, A.; Gonçalves Cardoso, S.; Rodríguez-Hornedo, N. Cocrystals to facilitate delivery of poorly soluble compounds beyond-rule-of-5. *Adv. Drug Delivery Rev.* **2016**, *101*, 143−166.
(9) McNamara, D. P.; Childs, S. L.; Giordano, J.; Iarriccio, A.; Cassidy, J.; Shet, M. S.; Mannion, R.; O'Donnell, E.; Park, A. Use of a glutaric acid cocrystal to improve oral bioavailability of a low aolubility API. *Pharm. Res.* **2006**, *23*, 1888−1897.
(10) Roy, S.; Quiñones, R.; Matzger, A. J. Structural and physicochemical aspects of dasatinib hydrate and anhydrate phases. *Cryst. Growth Des.* **2012**, *12*, 2122−2126.
(11) Abdelgalil, A. A.; Al-Kahtani, H. M.; Al-Jenoobi, F. I. Chapter Four - Erlotinib. In *Profiles of Drug Substances, Excipients and Related Methodology*, Brittain, H. G., Ed.; Academic Press, 2020, Vol. *45*, pp. 93−117.
(12) *World Health Organization Model List of Essential Medicines 22nd List*; World Health Organization, Geneva, 2021. https://www.who.int/publications/i/item/WHO-MHP-HPS-EML-2021.02.
(13) Thorat, S. H.; George, C. P.; Shaligram, P. S.; Suresha, P. R.; Gonnade, R. J. Polymorphs and hydrates of the anticancer drug erlotinib: X-ray crystallography, phase transition and biopharmaceutical studies. *CrystEngcomm* **2021**, *23* (22), 3961−3974.
(14) António, C. T.; Évora, A. O. L.; Bernardes, C. E. S.; Diogo, H. P.; de Araujo, G. L. B.; Smith, P.; Byrn, S. R.; Fausto, R.; Minas da Piedade, M. E. Polymorphism in erlotinib hydrochloride: new insights into relative stability, thermal behavior, and structural differences of forms A and B. *Cryst. Growth Des.* **2023**, *23*, 7374−7384.
(15) Sanphui, P.; Rajput, L.; Gopi, S. P.; Desiraju, G. R. New multicomponent solid forms of anti-cancer drug erlotinib: role of auxiliary interactions in determining a preferred conformation. *Acta Crystallogr., Sect. B* **2016**, *72*, 291−300.
(16) Prasad, R. J.; Satya, B. R. A. K.; Chowdary, N. V. *Polymorphs of erlotinib hydrochloride and method of preparation*. U.S. Patent 8,349,855 B2, 2013.
(17) Gavenda, A.; Vraspir, P.; Canavesi, A.; Aronhime, J.; Bigatti, E.; Faustmann, J.; Jegorov, A.; Stephens, P. W.; Lux, G.; Paiocchi, M. *Crystalline forms of erlotinib base and erlotinib HCl*. U.S> Patent 20,100,004,449 A1, 2010.
(18) Reddy, B. P.; Reddy, K. R.; Reddy, R. R.; Reddy, D. M.; Rao, T. S. *A novel hydrated form of erlotinib free base and a process for preparation of erlotinib hydrochloride polymorph form A substantially free of polymorph form B*, EP 2176241 B1, 2015.
(19) Bubendorf, A. G.; Hennig, M.; Hidber, P.; Rimmler, G.; Rohrer, F. *Polymorph of {6,7-bis(2-methoxy-ethoxy)-quinazolin-4yl}-(3E)*, EP 1597239 B2, 2022.
(20) Winter, S.; Yongyan, S.; Talavera, E. P.; Berenguer, M. R.; Guorong, Z. *Method for preparing crystal form F of erlotinib HCl*, WO 2014190804 A1, 2015.
(21) Prasad, R. J.; Satya, B. R. A. K.; Chowdary, N. V. *Novel polymorphs of erlotinib hydrochloride and method of preparation*, EP2170844A1, 2010.
(22) Tien, Y.-C.; Su, C.-S.; Lien, L.-H.; Chen, Y.-P. Recrystallization of erlotinib hydrochloride and fulvestrant using supercritical antisolvent process. *J. Supercrit. Fluids* **2010**, *55*, 292−299.
(23) Selvanayagam, S.; Sridharb, B.; Ravikumarb, K. Erlotinib hydrochloride: an anticancer agent. *Acta Crystallogr. Sect. E* **2008**, *64* (5), o931.
(24) Rao, D. R.; Kankan, R. N. *Process for preparation of erlotinib and its pharmaceutically acceptable salts*, WO 2008122776 A2, 2008.
(25) Maocong, Y.; Qingshuang, M.; Xinyu, Z.; Zhaotao, Y. *The preparation method of erlotinib hydrochloride form B*, CN 2013102781082 A, 2013.
(26) Sridhar, B.; Ravikumar, K.; Krishnan, H.; Singh, A. N. Multicomponent crystals of erlotinib. *Acta Crystallogr., Sect. C* **2010**, *66*, o33−o38.
(27) Huang, L. *Amorphous forms of erlotinib hydrochloride and its solid amorphous dispersion*. U.S. Patent 7,625,911 B2, 2009.
(28) Bazaei, M.; Honarvar, B.; Esfandiari, N.; Sajadian, S. A.; Aboosadi, Z. A. Preparation of Erlotinib hydrochloride nanoparticles (anti-cancer drug) by RESS-C method and investigating the effective parameters. *Sci. Rep.* **2024**, *14* (1), 14955.
(29) Jia, S.; Ning, S.; Leng, Y.; Jing, Q.; Xu, Z.; Ren, F. Stabilizing effect of soluplus on erlotinib metastable crystal form in microparticles and amorphous solid dispersions. *Polymers* **2022**, *14*, 1241.
(30) Jahangiri, A.; Khalilzad, F.; Barghi, L. Dissolution improvement of binary solid dispersions of erlotinib prepared by one-step electrospray method. *Biol. Methods Protoc.* **2022**, *7* (1), bpac001.
(31) Mugnier, L.; Espitalier, F.; Menegotto, J.; Bell, S.; Ré, M. I. Solid amorphous formulations for enhancing solubility and inhibiting erlotinib crystallization during gastric-to-intestinal transfer. *Pharm. Dev. Technol.* **2023**, *28*, 697−707.
(32) Lu, J.; Zhan, X.; Chen, L.; Zhang, L.; Mao, S. Solubility of two polymorphs of erlotinib hydrochloride in isopropanol and acetone from (273.15 to 303.15) K. *J. Chem. Eng. Data* **2014**, *59*, 2665−2669.
(33) Zhai, J.; Zhao, J.; Chen, Z.; Xiao, C.; Liu, X.; Zhang, L.; Lu, J. Solubility measurement and correlation of two erlotinib hydrochloride polymorphs in alcohols and ketones from 273.15 to 323.15 K. *J. Chem. Eng. Data* **2017**, *62*, 516−524.
(34) Williams, H. D.; Ford, L.; Han, S.; Tangso, K. J.; Lim, S.; Shackleford, D. M.; Vodak, D. T.; Benameur, H.; Pouton, C. W.; Scammells, P. J. Enhancing the oral absorption of kinase Inhibitors using lipophilic salts and lipid-based formulations. *Mol. Pharmaceutics* **2018**, *15*, 5678−5696.
(35) Dora, C. P.; Kushwah, V.; Katiyar, S. S.; Kumar, P.; Pillay, V.; Suresh, S.; Jain, S. Improved oral bioavailability and therapeutic efficacy of erlotinib through molecular complexation with phospholipid. *Int. J. Pharm.* **2017**, *534*, 1−13.
(36) Truong, D. H.; Tran, T. H.; Ramasamy, T.; Choi, J. Y.; Lee, H. H.; Moon, C.; Choi, H.-G.; Yong, C. S.; Kim, J. O. Development of solid self-emulsifying formulation for improving the oral bioavailability of erlotinib. *AAPS PharmScitech* **2016**, *17*, 466−473.
(37) Dora, C. P.; Trotta, F.; Kushwah, V.; Devasari, N.; Singh, C.; Suresh, S.; Jain, S. Potential of erlotinib cyclodextrin nanosponge complex to enhance solubility, dissolution rate, *in vitro* cytotoxicity and oral bioavailability. *Carbohydr. Polym.* **2016**, *137*, 339−349.
(38) Erdoğar, N.; Akkın, S.; Varan, G.; Bilensoy, E. Erlotinib complexation with randomly methylated β-cyclodextrin improves drug solubility, intestinal permeability, and therapeutic efficacy in non-small cell lung cancer. *Pharm. Dev. Technol.* **2021**, *26*, 797−806.
(39) Fernandez, L. A.; Guillan, M. G.; Murpani, D.; Martinez, M. V. *Pharmaceutical composition comprising erlotinib hydrochloride*, WO 2016082879 A1, 2016.
(40) Wang, H.; Lai, Y.; Li, D.; Karges, J.; Zhang, P.; Huang, H. Self-assembly of erlotinib-platinum(II) complexes for epidermal growth factor receptor-targeted photodynamic therapy. *J. Med. Chem.* **2024**, *67*, 1336−1346.
(41) Dwivedi, N.; Panja, S. K.; Monika; Saha, S.; Sunkari, S. S. Anion directed structural diversity in zinc complexes with conformationally flexible quinazoline ligand: structural, spectral and theoretical studies. *Dalton Trans.* **2016**, *45* (30), 12053−12068.
(42) Kumar, R.; Thakur, A.; Sachin; Chandra, D.; Verma, A. K.; Dhiman, P. K.; Sharma, U. Quinoline-based metal complexes: synthesis and applications. *Coord. Chem. Rev.* **2024**, *499*, 215453.
(43) Kakoulidou, C.; Chasapis, C. T.; Hatzidimitriou, A. G.; Fylaktakidou, K. C.; Psomas, G. Transition metal(ii) complexes of halogenated derivatives of (E)-4-(2-(pyridin-2-ylmethylene)-hydrazinyl)quinazoline: structure, antioxidant activity, DNA-binding DNA photocleavage, interaction with albumin and in silico studies. *Dalton Trans.* **2022**, *51*, 16688−16705.
(44) Lipunova, G. N.; Nosova, E. V.; Charushin, V. N.; Chupakhin, O. N. Structural, optical properties, and biological activity of complexes based on derivatives of quinoline, quinoxaline, and quinazoline with metal centers from across the periodic table. *Comments Inorg. Chem.* **2014**, *34*, 142−177.
(45) Vogt, F. G. Solid-State NMR in Drug Discovery and Development. In *New Applications of NMR in Drug Discovery and Development*, Garrido, L.; Beckmann, N., Eds.; The Royal Society of Chemistry, 2013.

https://doi.org/10.1021/acs.cgd.5c00268
Cryst. Growth Des. 2025, 25, 3219−3228

(46) Li, M.; Xu, W.; Su, Y. Solid-state NMR spectroscopy in pharmaceutical sciences. *Trends Anal. Chem.* **2021**, *135*, 116152.
(47) Berendt, R. T.; Sperger, D. M.; Munson, E. J.; Isbester, P. K. Solid-state NMR spectroscopy in pharmaceutical research and analysis. *Trends Anal. Chem.* **2006**, *25*, 977−984.
(48) Geppi, M.; Mollica, G.; Borsacchi, S.; Veracini, C. A. Solid-state NMR studies of pharmaceutical systems. *Appl. Spectrosc. Rev.* **2008**, *43*, 202−302.
(49) Tishmack, P. A.; Bugay, D. E.; Byrn, S. R. Solid-state nuclear magnetic resonance spectroscopy-pharmaceutical applications. *J. Pharm. Sci.* **2003**, *92*, 441−474.
(50) Lutker, K. M.; Quiñones, R.; Xu, J.; Ramamoorthy, A.; Matzger, A. J. Polymorphs and hydrates of acyclovir. *J. Pharm. Sci.* **2011**, *100*, 949−963.
(51) Holmes, S. T.; Wang, W. D.; Hou, G.; Dybowski, C.; Wang, W.; Bai, S. A new NMR crystallographic approach to reveal the calcium local structure of atorvastatin calcium. *Phys. Chem. Chem. Phys.* **2019**, *21*, 6319−6326.
(52) Hirsh, D. A.; Holmes, S. T.; Chakravarty, P.; Peach, A. A.; DiPasquale, A. G.; Nagapudi, K.; Schurko, R. W. *In situ* characterization of waters of hydration in a variable-hydrate active pharmaceutical ingredient ssing ^{35}Cl solid-state NMR and X-ray diffraction. *Cryst. Growth Des.* **2019**, *19*, 7349−7362.
(53) Peach, A. A.; Fleischer, C. H.; Levin, K.; Holmes, S. T.; Sanchez, J. E.; Schurko, R. W. Quadrupolar NMR crystallography guided crystal structure prediction (QNMRX-CSP). *CrystEngcomm* **2024**, *26*, 4782−4803.
(54) Hartman, J. D.; Day, G. M.; Beran, G. J. O. Enhanced NMR discrimination of pharmaceutically relevant molecular crystal forms through fragment-based ab initio chemical shift predictions. *Cryst. Growth Des.* **2016**, *16*, 6479−6493.
(55) Ramos, S. A.; Mueller, L. J.; Beran, G. J. O. The interplay of density functional selection and crystal structure for accurate NMR chemical shift predictions. *Faraday Discuss* **2025**, *255*, 119−142.
(56) Fleischer, C. H., III; Holmes, S. T.; Levin, K.; Veinberg, S. L.; Schurko, R. W. Characterization of ephedrine HCl and pseudoephedrine HCl using quadrupolar NMR crystallography guided crystal structure prediction. *Faraday Discuss* **2025**, *255*, 88−118.
(57) Stirk, A. J.; Holmes, S. T.; Souza, F. E. S.; Hung, I.; Gan, Z.; Britten, J. F.; Rey, A. W.; Schurko, R. W. An unusual ionic cocrystal of ponatinib hydrochloride: characterization by single-crystal X-ray diffraction and ultra-high field NMR spectroscopy. *CrystEngcomm* **2024**, *26*, 1219−1233.
(58) Holmes, S. T.; Vojvodin, C. S.; Schurko, R. W. Dispersion-corrected DFT methods for applications in nuclear magnetic resonance crystallography. *J. Phys. Chem. A* **2020**, *124*, 10312−10323.
(59) Kalakewich, K.; Iuliucci, R.; Mueller, K. T.; Eloranta, H.; Harper, J. K. Monitoring the refinement of crystal structures with ^{15}N solid-state NMR shift tensor data. *J. Chem. Phys.* **2015**, *143* (19), 194702.
(60) Harper, J. K.; Iuliucci, R.; Gruber, M.; Kalakewich, K. Refining crystal structures with experimental ^{13}C NMR shift tensors and lattice-including electronic structure methods. *CrystEngcomm* **2013**, *15*, 8693−8704.
(61) Hildebrand, M.; Hamaed, H.; Namespetra, A. M.; Donohue, J. M.; Fu, R.; Hung, I.; Gan, Z.; Schurko, R. W. ^{35}Cl solid-state NMR of HCl salts of active pharmaceutical ingredients: structural prediction, spectral fingerprinting and polymorph recognition. *CrystEngcomm* **2014**, *16*, 7334−7356.
(62) Vojvodin, C. S.; Holmes, S. T.; Watanabe, L. K.; Rawson, J. M.; Schurko, R. W. Multi-component crystals containing urea: mechanochemical synthesis and characterization by ^{35}Cl solid-state NMR spectroscopy and DFT calculations. *CrystEngcomm* **2022**, *24*, 2626−2641.
(63) Hamaed, H.; Pawlowski, J. M.; Cooper, B. F. T.; Fu, R.; Eichhorn, S. H.; Schurko, R. W. Application of solid-state ^{35}Cl NMR to the structural characterization of hydrochloride pharmaceuticals and their polymorphs. *J. Am. Chem. Soc.* **2008**, *130*, 11056−11065.
(64) Holmes, S. T.; Hook, J. M.; Schurko, R. W. Nutraceuticals in bulk and dosage forms: analysis by ^{35}Cl and ^{14}N solid-state NMR and DFT calculations. *Mol. Pharmaceutics* **2022**, *19*, 440−455.
(65) Dolomanov, O. V.; Bourhis, L. J.; Gildea, R. J.; Howard, J. A. K.; Puschmann, H. OLEX2: a complete structure solution, refinement and analysis program. *J. Appl. Crystallogr.* **2009**, *42* (2), 339−341.
(66) Sheldrick, G. M. SHELXT - integrated space-group and crystal-structure determination. *Acta Crystallogr., Sect. A: Found. Adv.* **2015**, *71*, 3−8.
(67) Sheldrick, G. M. Crystal structure refinement with SHELXL. *Acta Crystallogr., Sect. C* **2015**, *71* (1), 3−8.
(68) Fu, R.; Brey, W. W.; Shetty, K.; Gor'kov, P.; Saha, S.; Long, J. R.; Grant, S. C.; Chekmenev, E. Y.; Hu, J.; Gan, Z. Ultra-wide bore 900 MHz high-resolution NMR at the National High Magnetic Field Laboratory. *J. Magn. Reson.* **2005**, *177*, 1−8.
(69) van Meerten, S. G. J.; Franssen, W. M. J.; Kentgens, A. P. M. ssNake: a cross-platform open-source NMR data processing and fitting application. *J. Magn. Reson.* **2019**, *301*, 56−66.
(70) Clark, S. J.; Segall, M. D.; Pickard, C. J.; Hasnip, P. J.; Probert, M. J.; Refson, K.; Payne, M. C. First principles methods using CASTEP. *Z. Kristallogr.* **2005**, *220*, 567−570.
(71) Te Velde, G.; Bickelhaupt, F. M.; Baerends, E. J.; Fonseca Guerra, C.; van Gisbergen, S. J. A.; Snijders, J. G.; Ziegler, T. Chemistry with ADF. *J. Comput. Chem.* **2001**, *22*, 931−967.
(72) Oswald, H. R.; Jaggi, H. Zur Struktur der wasserfreien Zinkhalogenide I. Die wasserfreien Zinkchloride. *Helv. Chim. Acta* **1960**, *43*, 72−77.
(73) Bryce, D. L. NMR crystallography: structure and properties of materials from solid-state nuclear magnetic resonance observables. *IucrJ* **2017**, *4*, 350−359.
(74) Soss, S. E.; Flynn, P. F.; Iuliucci, R. J.; Young, R. P.; Mueller, L. J.; Hartman, J.; Beran, G. J. O.; Harper, J. K. Measuring and modeling highly accurate ^{15}N chemical shift tensors in a peptide. *ChemPhyschem* **2017**, *18*, 2225−2232.
(75) Holmes, S. T.; Iuliucci, R. J.; Mueller, K. T.; Dybowski, C. Critical analysis of cluster models and exchange-correlation functionals for calculating magnetic shielding in molecular solids. *J. Chem. Theory Comput.* **2015**, *11*, 5229−5241.
(76) Toomey, R.; Wang, L.; Heider, E. C.; Hartman, J. D.; Nichols, A. J.; Myles, D. A. A.; Gardberg, A. S.; McIntyre, G. J.; Zeller, M.; Mehta, M. A. NMR-guided refinement of crystal structures using ^{15}N chemical shift tensors. *CrystEngcomm* **2024**, *26*, 3289−3302.
(77) Hartman, J. D.; Kudla, R. A.; Day, G. M.; Mueller, L. J.; Beran, G. J. O. Benchmark fragment-based ^{1}H, ^{13}C, ^{15}N and ^{17}O chemical shift predictions in molecular crystals. *Phys. Chem. Chem. Phys.* **2016**, *18*, 21686−21709.
(78) Alderman, D. W.; Sherwood, M. H.; Grant, D. M. Comparing, modeling, and assigning chemical-shift tensors in the cartesian, irreducible spherical, and icosahedral representations. *J. Magn. Reson.* **1993**, *101*, 188−197.
(79) O'Dell, L. A.; Schurko, R. W. QCPMG using adiabatic pulses for faster acquisition of ultra-wideline NMR spectra. *Chem. Phys. Lett.* **2008**, *464*, 97−102.
(80) O'Dell, L. A.; Rossini, A. J.; Schurko, R. W. Acquisition of ultra-wideline NMR spectra from quadrupolar nuclei by frequency stepped WURST−QCPMG. *Chem. Phys. Lett.* **2009**, *468*, 330−335.
(81) Schurko, R. W. Ultra-wideline solid-state NMR spectroscopy. *Acc. Chem. Res.* **2013**, *46*, 1985−1995.
(82) Rossini, A. J.; Mills, R. W.; Briscoe, G. A.; Norton, E. L.; Geier, S. J.; Hung, I.; Zheng, S.; Autschbach, J.; Schurko, R. W. Solid-state chlorine NMR of group IV transition metal organometallic complexes. *J. Am. Chem. Soc.* **2009**, *131*, 3317−3330.
(83) Lucier, B. E. G.; Reidel, A. R.; Schurko, R. W. Multinuclear solid-state NMR of square-planar platinum complexes — Cisplatin and related systems. *Can. J. Chem.* **2011**, *89*, 919−937.
(84) Lucier, B. E. G.; Johnston, K. E.; Xu, W.; Hanson, J. C.; Senanayake, S. D.; Yao, S.; Bourassa, M. W.; Srebro, M.; Autschbach, J.; Schurko, R. W. Unravelling the structure of Magnus. *Pink Salt. J. Am. Chem. Soc.* **2014**, *136*, 1333−1351.

https://doi.org/10.1021/acs.cgd.5c00268
Cryst. Growth Des. 2025, 25, 3219−3228

(85) O'Keefe, C. A.; Johnston, K. E.; Sutter, K.; Autschbach, J.; Gauvin, R.; Trébosc, J.; Delevoye, L.; Popoff, N.; Taoufik, M.; Oudatchin, K. An investigation of chlorine ligands in transition-metal complexes via ^{35}Cl solid-state NMR and density functional theory calculations. *Inorg. Chem.* **2014**, *53*, 9581−9597.
(86) Johnston, K. E.; O'Keefe, C. A.; Gauvin, R. M.; Trébosc, J.; Delevoye, L.; Amoureux, J.-P.; Popoff, N.; Taoufik, M.; Oudatchin, K.; Schurko, R. W. A study of transition-metal organometallic complexes combining ^{35}Cl solid-state NMR spectroscopy and ^{35}Cl NQR spectroscopy and first-principles DFT calculations. *Chem.- Eur. J.* **2013**, *19*, 12396−12414.
(87) Bauder, L.; Wu, G. Solid-state $^{35/37}$Cl NMR detection of chlorine atoms directly bound to paramagnetic cobalt(II) ions in powder samples. *Magn. Reson. Chem.* **2024**, *62*, 145−155.
(88) Zhang, W.; Lucier, B. E. G.; Willans, M. J.; Huang, Y. ^{35}Cl NMR of metal-organic frameworks: what can we learn? *Chem. Methods* **2025**, No. e202400078.
(89) Townes, C. H.; Dailey, B. P. Determination of electronic structure of molecules from nuclear quadrupole effects. *J. Chem. Phys.* **1949**, *17*, 782−796.
(90) Lipton, A. S.; Sears, J. A.; Ellis, P. D. A general strategy for the NMR observation of half-integer quadrupolar nuclei in dilute environments. *J. Magn. Reson.* **2001**, *151*, 48−59.
(91) Peach, A. A.; Hirsh, D. A.; Holmes, S. T.; Schurko, R. W. Mechanochemical syntheses and ^{35}Cl solid-state NMR characterization of fluoxetine HCl cocrystals. *CrystEngcomm* **2018**, *20*, 2780−2792.
(92) Vojvodin, C. S.; Holmes, S. T.; Kirschhock, C. E. A.; Hirsh, D. A.; Huskić, I.; Senanayake, S.; Betancourt, L.; Xu, W.; Breynaert, E.; Friščić, T. Rietveld refinement and NMR crystallographic investigations of multicomponent crystals containing alkali metal chlorides and urea. *J. Appl. Crystallogr.* **2025**, *58*, 333−348.

https://doi.org/10.1021/acs.cgd.5c00268
Cryst. Growth Des. 2025, 25, 3219−3228